0Physicochem. Probl. Miner. Process., 58(4), 2022, 150348

http://www.journalssystem.com/ppmp

Physicochemical Problems of Mineral Processing

ISSN 1643-1049

Structural and photocatalytic properties of Ni-TiO_2 photocatalysts prepared by mechanochemical synthesis assisted with calcination

Karolina Kucio, Barbara Charmas, Magdalena Zięzio, Sylwia Pasieczna-Patkowska

Institute of Chemical Sciences, Faculty of Chemistry, Maria Curie-Sklodowska University, Maria Curie-Sklodowska Sq. 3, 20-031 Lublin, Poland

Corresponding author: karolina.kucio@poczta.umcs.lublin.pl (Karolina Kucio)

Abstract: In the study the mechanochemical synthesis in the planetary ball mill was used to prepare photocatalytic materials obtained on the basis of TiO_2 and nickel(II) acetylacetonate as a Ni^{2+} source. Three materials with different contents of Ni^{2+}: 5, 10 and 20% wt. were prepared. The obtained materials were calcinated at 800°C for 1 h. Their physicochemical properties were investigated using the N_2 adsorption/desorption, FT-IR/PAS, XRD, UV-Vis/DRS and SEM methods. Additionally, thermal stability of the obtained materials was examined (TGA/DTG/DTA). Photocatalytic activity of the samples was tested in relation to the aqueous solution of Safranin T (initial concentration $C_0 = 1\times10^{-5}$ mol L^{-1}) at the visible light (Vis). The results indicate that the mechanochemical synthesis is an effective and simple method for preparing materials with photocatalytic properties. All obtained materials were characterized by greater photocatalytic activity compared to the initial TiO_2.

Keywords: mechanochemical synthesis, titanium dioxide, photocatalysis, photocatalysts, safranin T

1. Introduction

Water is an essential resource for the proper functioning of all living organisms. It should be clean, safe and pollutants free. It is estimated that only 0.007% of the Earth's water is available for consumption (Pandit and Kumar, 2019). Curently water pollution is one of the major having a significant impact on human health. This issue is becoming more serious and is caused by the population growth and the intensive development of industry (Ismail et al., 2019; Saini, 2017). Water pollution is mainly due to the presence of inter alia pathogenic bacteria (Zhou et al., 2020; Hashim et al., 2020), inorganic compounds such as salts (Long et al., 2020; Gutierrez et al., 2010), heavy metals (Barakat, 2011; Dean et al.,1972; Qdais and Moissa, 2004) and radioactive compounds (Awual et al., 2016; Khayet, 2013). Water pollutants are classified into: biological, physical and chemical ones. The last one is the most hazardous for the population. One of the main sources of chemical water pollution in the world is the textile industry which generates large amounts of wastewater containing organic dyes (Saini, 2017). This industrial sector is one of the world's biggest polluters and consumes large amounts of chemicals and fuels (Bhatia, 2017). Moreover, organic dyes are extensively used in many technological processes, including paper, food and cosmetic production. Dyes from the industry run off into rivers and wastewater affecting the quality of drinking water. Thus, water is unfit for human consumption and constitutes a health risk. The main goal is to remove all pollutants that have a negative impact on the environment and human life (Saini, 2017). Dyes are organic compounds characterized by great solubility in water (Mahapatra, 2016). There are many ways to remove organic dyes from water to reduce their impact on the environment (Forgacs et al., 2004). These methods include e.g: adsorption (Tan et al., 2015; Iqbal and Ashiq, 2007), chemical precipitation (Tan et al., 2000; Duan et al., 2020) or chemical oxidation (Türgay et al., 2011; Dutta et al., 2001). Unfortunately, they are characterized by high cost, low efficiency and limited versatility (Ali, 2010). Advanced oxidation processes (AOPs) are promising methods for removing organic compounds including dyes from wastewater. The main role is played by the heterogeneous photocatalysis and its action due to the solar light for wastewater

DOI: 10.37190/ppmp/150348

This article is an extended version of the papers published in a special issue entitled "The Symposium *Physicochemistry of Interfaces - Instrumental Methods*"

treatment (Viswanathan, 2018). This method is simple, cheap and easy. Generally, photocatalytic heterogeneous processes proceed in the aqueous phase in the presence of the photocatalyst. Molecules are absorbed on the photocatalyst surface and then they are oxidized to simple inorganic compounds. Semiconductors are often used as photocatalysts. These materials absorb photons whose energy is equal or higher than that of the semiconductor band gap resulting in the electron-hole pairs formation. The created electrons and holes generate reactive radicals causing dye degradation through the redox reactions. Their products are harmless to the environment (Rauf and Ashraf, 2009; Viswanathan, 2018). Heterogeneous photocatalysts based on TiO_2 have attracted a significant attention for wastewater treatment (Ammari et al., 2020; Farghali et al., 2016; Ajmal et al., 2014; Kucio et al., 2020). There are many methods for producing photocatalysts, e.g.: hydrothermal methods (Kolen’ko et al., 2004), co-precipitation (Sanchez-Martinez et al., 2018) or sol–gel (Anderson and Bard, 1995; Koe et al., 2019). However, these processes are characterized by large consumption of solvents and energy and usually generate high temperatures and pressures as well as a lot of dangerous by-products (Molchanov and Buyanov, 2001). The other method which enables synthesis of materials with photocatalytic activity is the mechanochemical synthesis also known as mechanical ball-milling (Kucio et al., 2019; Kucio et al., 2020). This method enables grinding powders into fine particles inducing formation of new chemical bonds and generating pores. Additionally, it is an environmentally friendly and cost-effective technique (Burmeister and Kwade, 2013). Mechanochemical synthesis does not require the use of toxic solvents and often eliminates completely the production of by-products which is compatible with the principles of green chemistry introduced by Anastas (Molchanov and Buyanov, 2001; Anastas and Kirchhoff, 2002). The novelty of this paper was using the mechanochemical synthesis for effective dopping of standard TiO_2 (P25) by Ni^{2+} ions to obtain the photocatalyst well working in the visible light region. The aim of this paper was to prepare materials with photocatalytic activity using the mechanochemical synthesis method in the high-energy planetary mill. The obtained materials contained TiO_2 and nickel acetylacetonate (Acac-Ni) as a source of nickel ions (dopant). Photocatalytic activity of the prepared materials was tested in relation to the aqueous solution of Safranin T (ST) in the range of visible light (Vis). The obtained materials were also subjected to structural characterization.

2. Materials and methods

2.1. Materials preparation

The materials used in the study were: TiO_2 (P-25, purity ≥99.5%, Sigma-Aldrich, Poland) and nickel(II) acetylacetonate (Acac-Ni, $C_{10}H_{14}NiO_4$, purity 95%, POCh, Poland) as a Ni^{2+} source. Photocatalysts were prepared by the mechanochemical synthesis (MChS) of the initial materials in a planetary ball mill (Pulverisette 7 Premium Line, Fritsch, Germany). Milling of powders was performed in the vessel made of Si_3N_4 ($V = 45\ cm^3$) which contained 25 balls (ø = 10 mm) made of the same material. The total balls mass was 40 g. The milling duration was 1 h (four cycles × 15 min, 5-min breaks were between the 15-min cycles) and the mill rotation speed was 250 rpm. The milling process took place with the redestilled water (30 ml) and then the obtained products were dried at 20°C for 48 h. Three materials with different nickel ions contents (Ni^{2+}): 5, 10, 20% wt. were prepared. Then the obtained materials were calcinated at 800°C for 1 h (Kosowska et al. 2005). The samples were designated as: $TN5_C$, $TN10_C$ and $TN20_C$ (Fig. 1). Additionally, the initial TiO_2 without the Ni^{2+} addition was subjected to the mechanochemical treatment (MChT) under the analogous conditions - TiO_2M (Fig. 1).

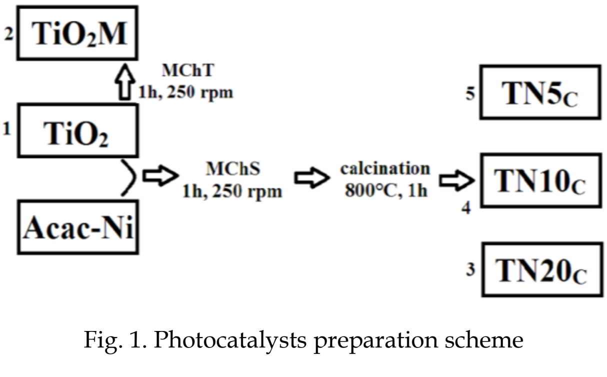

Fig. 1. Photocatalysts preparation scheme

2.2. Nitrogen adsorption/desorption

The structural parameters of the materials were determined by means of the nitrogen adsorption/desorption method at -196°C. The adsorption analyzer Micromeritics ASAP 2405N (USA) was applied for recording the adsorption isotherms. The specific surface area S_{BET} (BET equation at p/p_0 between 0.06 and 0.2) as well as the pore volume (V_p, $p/p_0 \approx 0.98$) were calculated from the obtained data (Gregg and Sing, 1982). The desorption isotherm data were used for determination of the pore size distributions ($f_V(R) \sim dV_p/dR$, PSD). There was also used the self-consistent regularization procedure (SCR) with the non-negative function of pore size distribution ($f(R_p) > 0$, $\alpha = 0.01$ as a fixed regularization parameter) (Gun'ko, 2014). Moreover, there was applied a model for the slit-like pores shape (S). The differential function was transformed into the incremental pore size distribution ($dV/dR = f(R)$, $IPSD_V$) based on the procedure presented by Gun'ko and Mikhalovsky (2004). The volume as well as the surface area for the mesopores (V_{meso}, S_{meso}) and the micropores (V_{micro}, S_{micro},) and the pore shape deviation (Δw) were calculated using the differential function (Table 1) (Charmas et al., 2017; Gun'ko and Do, 2001).

2.3. Scanning electron microscopy (SEM)

The morphology of the materials was analyzed using a DualBeam Quanta 3D FEG FEI. The quantitative and qualitative analyses were performed using the energy-dispersive X-ray spectroscopy (SEM/EDX, acceleration: 20 kV, magnifications x100000, x5000).

2.4. XRD analysis

Structural analysis of the materials was performed using the X-ray powder diffractometer (PANalytical, Empyrean, Netherlands) at the tension of 40 kV and the current of 10 mA. The monochromatic Cu Kα radiation ($\alpha = 1.5418$ Å) was used. The step-scanning mode ($\Delta 2\theta = 0.026°$) was applied in the angular 5–90° range for obtaining the patterns. The crystallite sizes of the photocatalysts were determined using the Rietveld method by means of the Scherrer equation from all diffraction lines (Holzwarth and Gibson, 2011).

2.5. Spectroscopic characterization (FT-IR/PAS)

Fourier transformed photoacoustic infrared spectra (FT-IR/PAS) of the examined samples were recorded by means of Bio-Rad Excalibur FT-IR 3000 MX spectrometer over the 3900-500 cm^{-1} range at room temperature, resolution 4 cm^{-1}, mirror velocity 2,5 kHz and maximum source aperture, using MTEC Model 300 photoacoustic cell. Dry helium was used to purge the photoacoustic cell before the data collection. The spectra were normalized by computing the ratio of a sample spectrum to that of the MTEC carbon black standard. A stainless steel cup (diameter 10 mm) was filled with the sample content without prior preparation (thickness <6 mm) and interferograms of 1024 scans were averaged for the spectrum, providing a good signal-to-noise (S/N) ratio. No smoothing functions were used. All spectral measurements were performed at least in triplicate.

2.6. Thermal analysis

Thermal properties of the samples were determined using a Derivatograph C (Paulik, Paulik & Erdey, MOM, Budapest). The tested materials (about 40 mg) were placed in a small corundum crucible. As a reference sample Al_2O_3 was used. The analysis was made in air atmosphere in the temperature range from 20 to 1000°C (heating rate 10°C min^{-1}). The TGA, DTG and DTA curves were registered.

2.7. Photocatalytic activity studies

Photocatalytic activity of the obtained samples was tested using the aqueous Safranin T (ST, C.I. 50240, Basic Red 2, $C_{20}H_{19}ClN_4$, purity 100%, Sigma-Aldrich, Poland), solution (initial concentration $C_0 = 1*10^{-5}$ mol L^{-1}, V=200 mL) in the range of visible light (Vis) at pH=6.5. The ratio of solution (ST) to the weight of tested sample was 1 ml : 1 mg (Sydorchuk et al., 2022; Bessekhouad et al., 2003; Kubiak et al., 2020). The ST solution with the tested photocatalyst was placed on the magnetic stirrer without light access for 30 min to determine the adsorption/desorption equilibrium of the dye on the photocatalyst surface. During the appropriate photocatalysis stage a proper amount of solution was taken at regular intervals (0.5; 1; 2; 3; 4; 5; 24 h) and next filtered using syringe filters and centrifuged to get rid of the photocatalyst. The photocatalysis stage was performed for 24 hours at room temperature for each sample. The LED electric bulb (14.5 W) which was located 20 cm above the surface of ST solution containing the photocatalyst was used as a source of visible light. The solution concentrations were measured using the UV-Vis spectrophotometer (Helios Gamma, Spectro-Lab, Poland) at λ=520 nm ($y = 0.2931x + 0.0126$; R^2=0.9992).

2.8. Statistical analysis

The results of the photocataytic test were demonstrated in the form of the mean deduced from three independent photocatalytic activity test (n=3). The results were compared based on the variance analysis (ANOVA, p= 0.05). The differences in the results proved to significant for $p < 0.05$ and $F_{exp} > F_{crit}$ (2.85). As followed from the variance analysis the differences were statistically significant for the materials being tested.

2.9. UV-Vis Diffuse Reflectance Spectroscopy

Diffuse reflectance UV–Vis spectra were obtained using the UV–Vis spectrophotometer (Carry 4000, Varian Inc., Australia) equipped with an integration sphere diffuse reflectance accessory. The spectra were measured at room temperature in the region λ= 200-800 nm. Diffuse reflectance spectra were recorded in order to calculate the band gap (E_g) of the materials according to the Kubelka-Munk method. E_g values were determined by plotting $(F(R) \cdot h\nu)^n$ versus hv. The band gap values were obtained by means of extrapolation according to the procedure used by López and Gomez (2012).

3. Results and discussion

3.1. Structural characteristics

Fig. 2 shows the low-temperature nitrogen adsorption/desorption isotherms (Fig. 2a) and the incremental pore volume distribution curves ($IPSD_V$) (Fig. 2b) for the all obtained materials as well as for the initial TiO_2 (P25) and TiO_2 after the mechanochemical treatment (TiO_2M). As follows from the analysis of the course of adsorption isotherms, they are of type IV according to the IUPAC classification (Rouquerol et al., 1994). This indicates that the obtained materials are mesoporous, in the pores of which the phenomenon of capillary condensation is observed (Rouquerol et al., 1994). The course of all isotherms is similar. Analyzing the shape of the curves, all isotherms in the area of relative pressure $p/p_0 < 0.1$ are located very low. This suggests that the number of micropores is negligible or absent

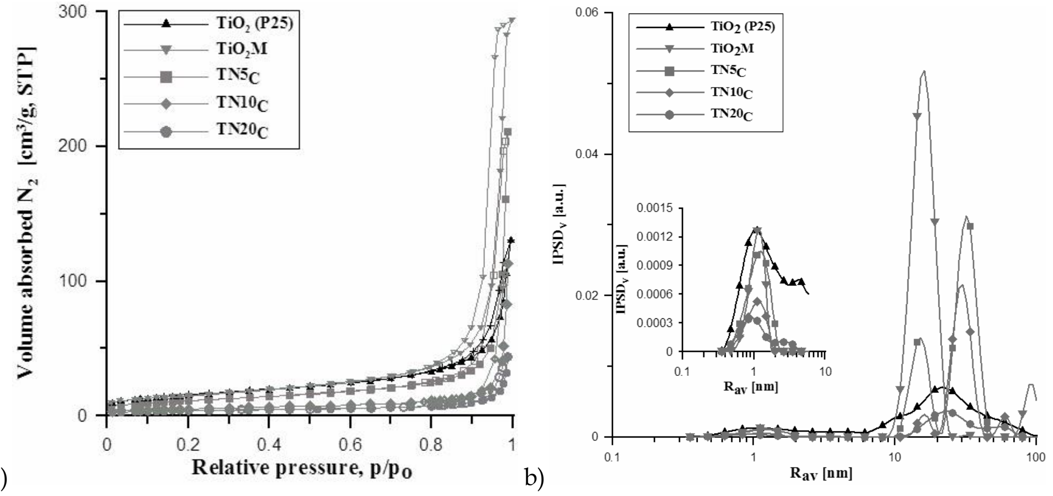

Fig. 2. Low-temperature nitrogen adsorption/desorption isotherms (a) and incremental pore volume distribution curves ($IPSD_V$) relative to their average radii (b) for all obtained materials, initial TiO_2 and that after the mechanochemical treatment TiO_2M

(Fig. 2a,b). For these materials the developed hysteresis loops are observed in the area of relative pressure p/p_0 = 0.8 - 1. These are H2 type hysteresis loops indicating that these materials contain mesopores in the slit shape (Gregg and Sing, 1982). The presence of mesopores in the obtained materials is confirmed by the curves shown in Fig. 2b which contain clearly defined maxima as well as the data included in Table 1.

The course of the isotherms presented in Fig. 2a shows that the mechanochemical treatment of the initial TiO_2 (TiO_2M) causes an intensive change in the structure compared to the initial TiO_2 (P25) (Table 1). The isotherm for the TiO_2M material is located much higher than that of the initial TiO_2 which indicates that the mechanochemical treatment resulted in the porous structure development. A well-formed hysteresis loop for this material suggests the mesopores formation (Fig. 2a). This effect is confirmed by the shape of the incremental pore volume distribution curve ($IPSD_V$) relative to their average radii where the maximum at R_{dom} ~ 16 nm indicates a significantly greater number (volume) of mesopores than in the case of the initial TiO_2 (Fig. 2b). For the initial TiO_2 the value of R_{dom} is approximately 22 nm (Fig. 2b, Table 1). Although the S_{BET} values of these materials are the same (Table 1), the pore volume (V_p) is more than twice larger for TiO_2 after the mechanochemical treatment (TiO_2M, Table 1). The $IPSD_V$ shape indicates that TiO_2M is a biporous material which is confirmed by the clearly developed maximum in the range of R_{av} = 10-25 nm and the maximum appearing in the area of macropores at R_{dom} = 90 nm (Fig. 2b). In the case of Ni^{2+} ions containing materials, it can be observed that with the increase in the content of nickel ions in the composites, the structural parameters decrease and the isotherms are located lower in relation to the axis of relative pressure (p/p_0) (Fig. 2a, Table 1). In the case of materials with the addition of nickel ions the most developed pore structure is observed in the sample with the smallest nickel ion content - $TN5_C$ (Fig. 2a). Therefore, as the content of Ni^{2+} increases, the isotherms are located lower but the hysteresis loops occur in a similar range of relative pressures. Fig. 2b shows that the increase in the Acac-Ni content results in a gradual decrease in the volume of pores V_p (Table 1). $TN5_C$ is a biporous material, which is evidenced by the clearly developed maxima in the area of mesopores (R_{dom} = 15 and 33nm). In the case of the $TN10_C$ and $TN20_C$ material the maxima occur in the area of mesopores (R_{dom} = 17 and 30 nm for $TN10_C$ and 26 nm for $TN20_C$) as well as in the area of macropores (R_{dom} = 60 nm for both materials) (Fig. 2b, Table 1). After calcination all obtained materials have a smaller value of S_{BET} compared to the initial TiO_2 (P25) (Table 1). The parameters presented in Table 1 confirm that the increase in the content of nickel ions causes a gradual reduction of the specific surface area S_{BET} and the sorption pores volume (V_p).

Table 1. Parameters of the porous structure for the initial TiO_2 (P25), TiO_2 after the mechanochemical treatment (TiO_2M) and the obtained samples

Sample	S_{BET} [m^2 g^{-1}]	S_{micro} [m^2 g^{-1}]	S_{meso} [m^2 g^{-1}]	S_{macro} [m^2 g^{-1}]	V_p [cm^3 g^{-1}]	V_{micro} [cm^3 g^{-1}]	V_{meso} [cm^3 g^{-1}]	V_{macro} [cm^3 g^{-1}]	R_{dom} [nm]	Δw
TiO_2(P25)	55	25	28	2	0.202	0.013	0.125	0.064	22	-0,485
TiO_2M	55	10	45	1	0.454	0.006	0.417	0.031	16;90	0.222
$TN5_C$	42	13	20	9	0.327	0.007	0.121	0.198	15;33	-0.041
$TN10_C$	19	7	7	5	0.175	0.004	0.048	0.124	17;30;60	-0.041
$TN20_C$	15	8	5	1	0.069	0.004	0.035	0.029	26;60	-0.431

S_{BET} - the specific surface area; S_{micro} - the surface area of micropores; S_{meso} - the surface area of mesopores; S_{macro} - the surface area of macropores; V_p - the sorption pores volume (from the N_2 desorption data); V_{micro} - the volume of micropores; V_{meso} - the volume of mesopores; V_{macro} - the volume of macropores; R_{dom} - the dominant pore radius; Δw - the deviation from the assumed pore model

The SEM images show that the initial TiO_2 (P25) structure is composed of individual, ordered globules with the homogeneous size about 40 nm (Fig. 3a). After the mechanochemical treatment of TiO_2 with the addition of nickel acetylacetonate (TN5, non-calcined material, Fig 3b,c), the structure of the material became less ordered. It can be seen the Acac-Ni particles in the form of flocs covered TiO_2 (Fig. 3b). After calcination ($TN5_C$, $TN20_C$, Fig. 3d,e) the structure became ordered. The organic components were partially burnt at 800°C which resulted in the absence of flocs (Fig. 3d,e) and the appearance of an altered structure of TiO_2. The TiO_2 globules were joined (sintering) and spatial structures containing wide pores were formed (Fig. 3d,e). This is confirmed by the curves shown in Fig. 2b (TiO_2 P25 and $TN5_C$). A similar relationship is observed in the case of the $TN20_C$ material. Increasing the dopant amount resulted in the increasing dominant pores sizes (Fig. 3 e, Table 1). Table 2 shows the EDS analysis results. As expected with the increasing Acac-Ni amount in the materials, the nickel amount increases while the Ti content decreases. In the SEM/EDS analysis, the entire area of the sample is not scanned, but the electron beam hits the sample pointwise, which explains the differences between the practical and theoretical Ni^{2+} contents in the materials.

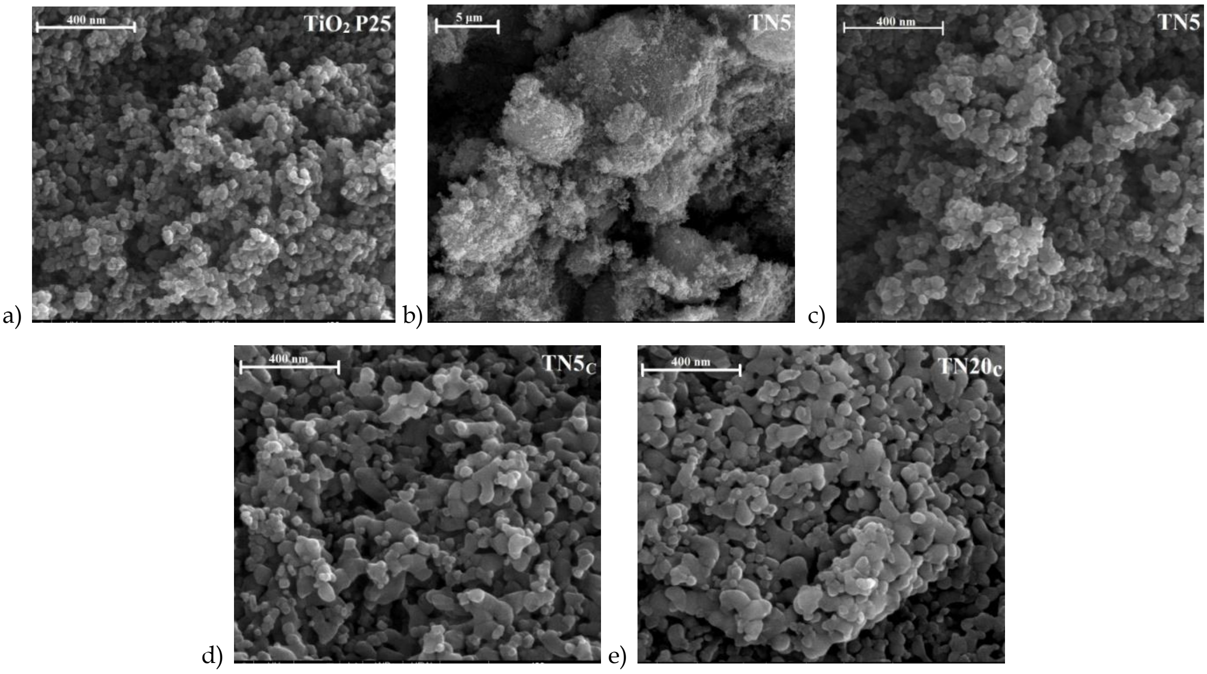

Fig. 3. SEM images for the initial TiO_2 P25 (a); TN5 (b,c); $TN5_C$ (d) and $TN20_C$ (e), magnifications x100000 (a,c,d,e) and x5000 (b)

Table 2. Results of SEM/EDS chemical composition microanalysis for the initial TiO_2(P25) and obtained samples

Element/Line [%wt.]	TiO_2(P25)	$TN5_C$	$TN10_C$	$TN20_C$
C/K	-	4.6	5.6	6.2
O/K	37.7	39.9	43.8	41.5
Ti/K	62.3	53.1	45.6	40.2
Ni/K	-	2.40	5.0	12.1

The XRD spectra of the tested photocatalysts show that the anatase and rutile phases are present in the samples (Table 3, Fig. 4). The initial TiO_2 (P25) consists of the mixed phases of 89% anatase and 11% rutile. The mechanochemical treatment of TiO_2 (TiO_2M) changes these values insignificantly. In the case of the nickel-doped materials, the formation of a new crystalline phase ($TiNiO_3$) was observed (JCPDS Card No. 04-006-6606). The confirmation of new crystalline phase presence are the peaks at $2\theta = 24.15°$, 33.11°, 35.70°, 49.46°. The calcination stage caused a decrease in the specific surface area of the materials (Table 1), as well as induced a phase change in the TiO_2 crystal forms (Table 3, Fig. 4). The data in Table 3 show a significant decrease in the anatase phase content from 89% for TiO_2 P25 to 13.8% for $TN5_C$, with a simultaneous intense increase in the share of the rutile phase from 11 to 76.5%. The crystal structure of the $TN5_C$ material after the calcination at 800°C contained small amounts of anatase while the rutile phase predominated as indicated by the peaks at $2\theta = 27.45°$, 36.08°, 41.24°, 44.06°, 54.33°, 56.65°, 65.53°, 69.02°, 69.80° (JCPDS Card No. 04-005-5127). Additionally, as a result of calcination at 800°C an increase in the size of anatase and rutile crystallites was observed. The transformation of the crystal structure from anatase to rutile at 800°C was also observed by Negishi and Takeuchi (1999). Similar results were obtained in the paper by Górska et al. (2008) where TiO_2 was calcined at 750°C. The authors (Górska et al., 2008) also observed that an increase in the calcination temperature causes a gradual increase in the size of both anatase and rutile crystallites. In the case of TN10$_C$ and TN20$_C$ samples, an increase in the $TiNiO_3$ phase was observed, which is related to the larger content of nickel ions in these materials compared to TN5$_C$ (Table 3).

The FT-IR/PAS spectra of the studied samples are presented in Fig. 5. The main bands at 3900-2400 cm^{-1} are the vibrations of hydroxyl groups in TiO_2. The band at 3689 cm^{-1} results from the isolated –OH in the oxide structure. The wide band with the maximum at ~ 3350 cm^{-1} shows the presence of both –OH and hydrogen bonded –OH···H in the TiO_2 structure and physically adsorbed water (Socrates, 2001). Observing the spectra in Fig. 5, one can notice a decrease in the intensity of the isolated hydroxyl groups bands along with an increase in the amount of the added nickel (samples TN5$_C$- TN20$_C$). This may indicate that the –OH groups are involved in metal ions binding with titanium oxide. Before the

Table 3. Physical properties of initial TiO_2(P25), TiO_2M and obtained samples.

Sample	Compound	TiO_2 crystalline form	Crystallite size [nm]	Crystalline phases of TiO_2 in material [%]
TiO_2 (P25)	Titanium dioxide	A R	23.3 36.8	89.0 11.0
TiO_2M	Titanium dioxide	A R	20.8 33.4	88.8 11.2
TN5$_C$	Titanium dioxide	A R	34.0 50.4	13.8 76.5
	Titanium nickel oxide	-	48.7	9.7
TN10$_C$	Titanium dioxide	A R	33.4 47.9	13.5 64.2
	Titanium nickel oxide	-	50.1	32.3
TN20$_C$	Titanium dioxide	A R	32.8 45.5	13.4 42.1
	Titanium nickel oxide	-	52.7	44.5

*A - anatase, R- rutile

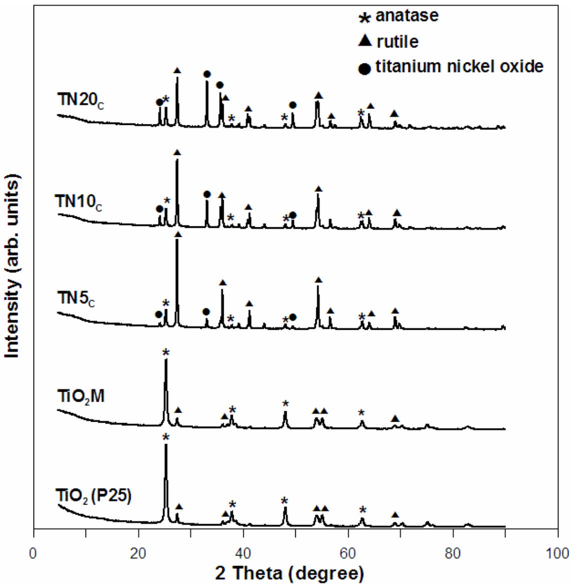

Fig. 4. XRD spectra registered for the initial TiO_2 (P25), TiO_2 after the mechanochemical treatment (TiO_2M) and obtained samples.

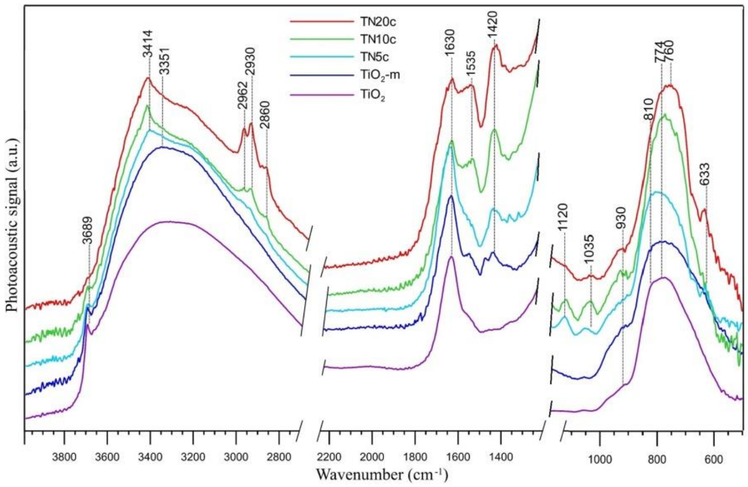

Fig. 5. FT-IR/PAS spectra of the studied samples in the 3900-500 cm^{-1} range

measurements, all samples were calcined, however, the presence of –CH groups bands in the range of 2962-2860 cm^{-1}, at 3414 cm^{-1} (intramolecular hydrogen bonded -OH groups from the nickel precursor) and at ~1535 cm^{-1} and 1420 cm^{-1} (C=O and –CH, respectively) may indicate incomplete removal of the organic part of the precursor during calcination. This can be confirmed by the presence of bands at 1120, 1035 and 633 cm^{-1} (C=O, -CH). The bands between 930 cm^{-1} and 500 cm^{-1} are a result of the Ti-O bond stretching. Slight shift of Ti-O vibrations from 774 to 760 cm^{-1} may be the result of Ni incorporation and hence changes in the TiO_6 octahedral arrangement (Hu et al. 2014). These changes well visible in the TN20C spectrum.

3.2. Thermal analysis

The thermal analysis was applied for estimation of the thermal stability of the materials. Fig. 6 shows the course of the TGA, DTG and DTA curves registered for the initial Acac-Ni (Fig. 6a) and TiO_2 after the mechanochemical treatment in the planetary ball mill (TiO_2M, Fig. 6b). In the case of Acac-Ni the recorded weight loss occurs in two stages, first in the range 20-200°C and the second 200-410°C. The first stage is associated with the desorption of physically bound water (20-200°C) and the weight loss is ~20 % up to 200°C (Fig. 6a). The second one is more intensive (~200°C- 410°C). In this stage the oxidative degradation of organic components occurs and the residue is NiO (Nichio et al., 2003). During this stage the heat is released (exothermic process). The total weight loss for this material is ~78% (Fig. 6a). Above the temperature 410°C no changes were observed. For the TiO_2M sample the total weight loss at ~1000°C is about 2.2% related to the desorption of the surface hydroxyl groups (Fig. 6b).

Fig. 7 shows the results of thermal analysis registered for the prepared materials and the initial

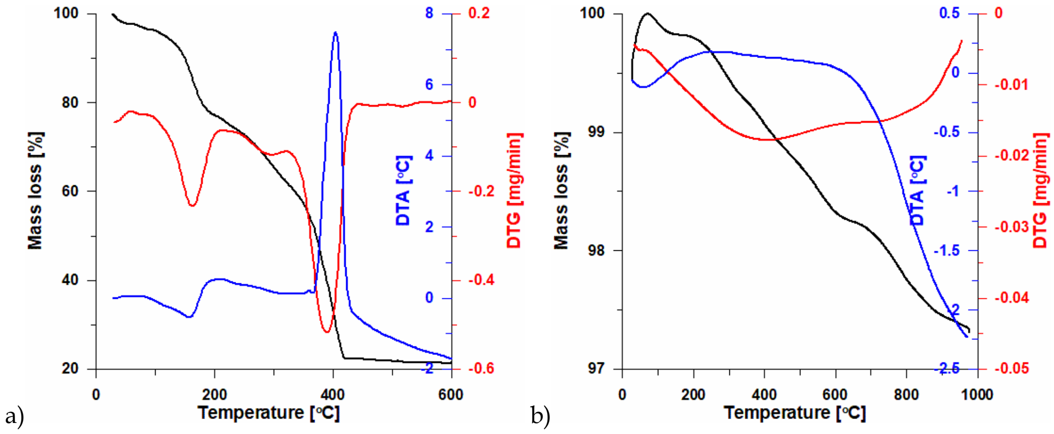

a) b)

Fig. 6. Courses of TGA, DTG and DTA curves for the initial Acac-Ni (a) and TiO_2 after the mechanochemical treatment in the planetary ball mill (TiO_2M)

materials before the calcinations stage (TN5, TN10, TN20). In the case of calcined materials ($TN5_C$, $TN10_C$, $TN20_C$) the weight loss of the samples was negligible. This is due to the earlier calcination in the air atmosphere during which combustion of Acac-Ni organic components took place. A very small weight loss (in the range 1-2%) results from the desorption of moisture adsorbed by the materials in the preparation stage of the samples for analysis (Fig. 7a). In the case of non-calcined materials the weight loss is clearly related to the combustion of Acac-Ni organic components. The temperature ranges in which weight changes take place are similar to those presented in Fig. 6a. The total weight loss depended on the Acac-Ni content in the composite. For the non-calcined materials these values are ~12% (TN5), ~20% (TN10) and ~42% (TN20). The higher the Acac-Ni content in the material, the greater the weight loss is observed. This is also confirmed by the changes shown on the DTG (Fig. 7b) and DTA curves (Fig. 7c).

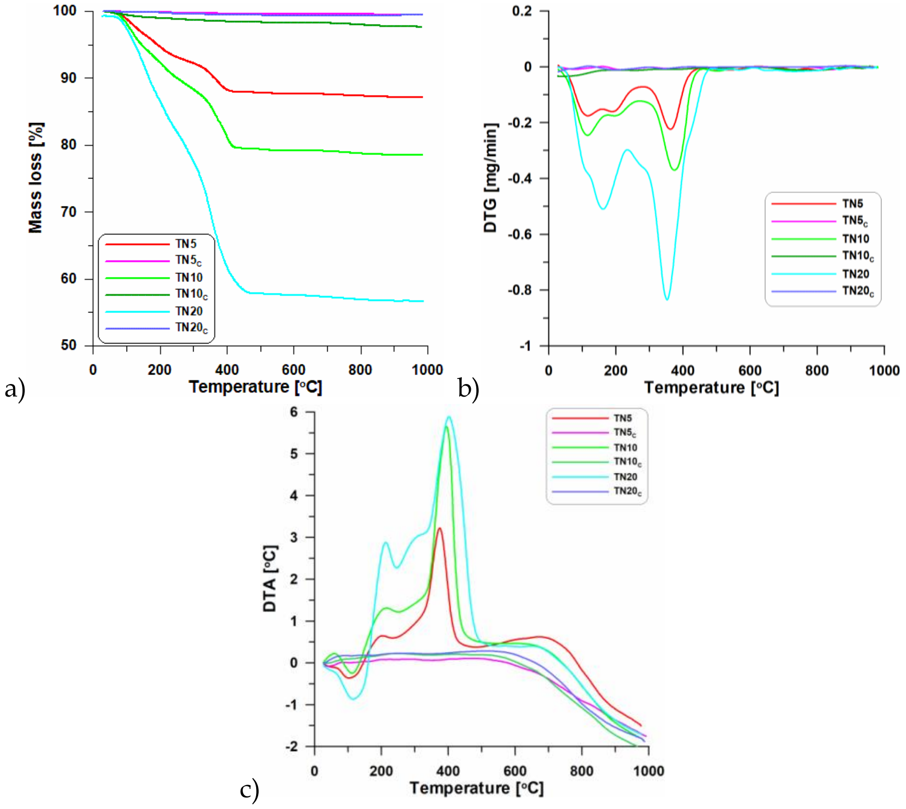

Fig. 7. Courses of TGA (a), DTG (b) and DTA (c) curves for the obtained materials ($TN5_C$, $TN10_C$, $TN20_C$) as well as those non-calcined (TN5, TN10, TN20)

3.3. Photocatalytic tests

Photocatalytic tests were carried out for all materials. During the measurments the dye adsorption stage on the material was performed. After 30 minutes in the dark, different Safranin T adsorptions were registered on the photocatalysts surface (Fig. 8). The course of the analyzed curves indicates that the greatest adsorption (~37%) was observed for the $TN20_C$ sample, where the dopant amount was the highest. This may result from the formation of strong coordination complexes between the amino groups present in the structure of the dye molecules with nickel ions occuring in the $TN20_C$ material (12.1%, Table 2, Chavan, 2011). In the case of the $TN5_C$ and $TN10_C$ samples the degree of adsorption was almost the same (~ 28%). The mechanochemical modification did not cause a significant change in the S_{BET} value, therefore the degree of dye adsorption for TiO_2M (29.5%, Fig. 8) was similar to that of the initial TiO_2 (31.8%, Fig. 8).

Fig. 9 presents the changes in the concentration of Safranin T solution irradiated with visible light (Vis) in the presence of the obtained materials after 24 hours. The Safranin T concentration after the adsorption as the initial concentration of the dye in the photocatalysis step was used. This action allowed studying of the actual photocatalytic activity of the obtained materials. The course of the curves shows that all obtained materials accelerated significantly the efficiency of Safranin T degradation and exhibited better photocatalytic properties compared to the initial TiO_2. In the case of the dye solution irradiated with visible light without the addition of a photocatalyst, its photolysis ~11% can be observed (Fig. 9).

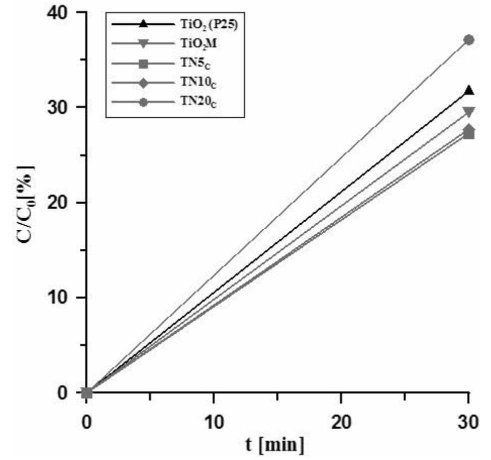

Fig. 8. Changes in the dye concentration (ST) after the 30-minute adsorption process on the tested photocatalysts in the dark

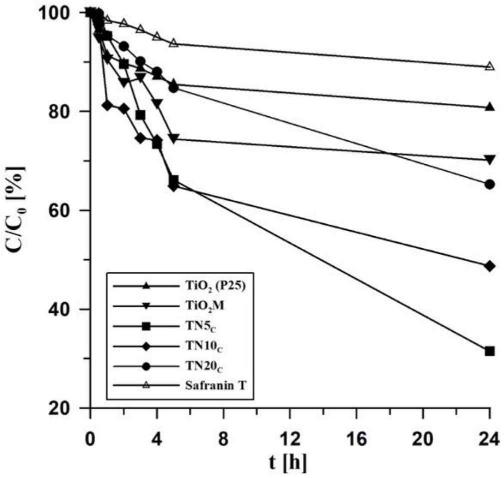

Fig. 9. Changes in the dye concentration (ST) during photocatalysis in the presence of all materials due to the visible light

The experiment was conducted for 24 hours. The first stage of dye degradation was more intense than the second one and lasted 5 hours. In the second stage the reduction of ST concentration was systematic and slow. After the mechanochemical treatment TiO_2 (TiO_2M) caused much more degradation of the dye (29.9%) than the starting TiO_2 (19.3%) (Fig. 9, Table 4). All obtained materials resulted in greater photocatalytic activity compared to that of the initial TiO_2 (P25). The $TN5_C$ proved to be the most effective. After the 24-hour exposure in the presence of this material the ST degradation was 68.5% (Fig. 9, Table 4). The variance analysis also showed that in the case of the $TN5_C$ sample, the greatest effect of time on the photocatalytic activity of the material was observed, F_{exp} = 278.83 (Table 5). In the case of the material with a larger content of Ni^{2+} ions ($TN10_C$, $TN20_C$), the degree of ST degradation was smaller. For $TN20_C$ the degree of dye degradation was twice smaller compared to that of the $TN5_C$ sample (Fig. 9, Table 4). Too large content of nickel ions could block the active centers of TiO_2 which are responsible for dye molecules binding and degradation. It should be noted that the material with the largest dopant amount ($TN20_C$) showed the best adsorption properties (Fig. 8), however, after calcination its photocatalytic activity was the smallest of the obtained materials (Fig. 9, Table 4). A significant amount of the dopant can constitute additional adsorption centers to trap the dye particles, simultaneously causing the TiO_2 matrix to be shielded, which has the effect of the material photoactivity constraint (Fig. 9) (Zaleska, 2008).

Table 4. Efficiency of the ST degradation [%] in the presence of the initial TiO_2 (P25) and obtained materials.

	Sample	TiO_2 (P25)	TiO_2M	$TN5_C$	$TN10_C$	$TN20_C$
Safranin T degradation [%]	after 5 hours	14.5	25.6	33.8	35.1	15.2
	after 24 hours	19.3	29.9	68.5	51.3	34.8

Table 5. Values of F and p from the variance analysis (F_{crit}= 2.85)

Sample	F_{exp}	p
TiO_2 (P25)	10.22	$1.9 * 10^{-4}$
TiO_2M	36.08	$9.85 * 10^{-8}$
$TN5_C$	278.83	$9.62 * 10^{-14}$
$TN10_C$	132.39	$1.63 * 10^{-11}$
$TN20_C$	53.27	$7.65 * 10^{-9}$

The Safranin T degradation could be explained by the following mechanism:

$$\text{Photocatalyst} + hv \rightarrow e^-_{CB} + h^+_{VB} \quad (1)$$

$$e^-_{CB} + O_2 \rightarrow {}^{\bullet}O_2^- \quad (2)$$

$$h^+_{VB} + H_2O \rightarrow {}^{\bullet}OH \quad (3)$$

$${}^{\bullet}O_2^- + {}^{\bullet}OH + \text{Safranin T} \rightarrow \text{degradation products} \quad (4)$$

When the photocatalyst in the solution was irradiated with light of greater energy than that of the band gap (Eq. 1), the electron (e^-) was excited in the conduction band (CB) and a hole (h^+) was created in the valence band (VB). The generated charge carriers migrated to the surface of the photocatalyst initiating redox reactions with the substrates adsorbed on the photocatalyst surface. The photo-excited electrons could react with oxygen molecules to form superoxide radicals (${}^{\bullet}O_2^-$) (Eq. 2). The electron holes could directly oxidize the dye molecules or react with the water molecules to form hydroxyl radicals (${}^{\bullet}OH$) (Eq. 3), which have strong oxidizing properties. Perhaps Safranin T is directly degraded by the produced radicals (${}^{\bullet}O_2^-$ i ${}^{\bullet}OH$) (Eq. 4).

The UV-Vis/DRS spectra (Fig. 10) were analyzed according to the Kulbelka–Munk (KM) method in order to calculate the band gap (E_g) of samples. According to the results presented in Table 6, the $TN5_C$ sample with the smallest value of band gap E_g = 2.94 eV showed the greatest activity. Thus, the amount of dopant plays an important role in creating TiO_2 photocatlitic activity. Also, the use of mechano-

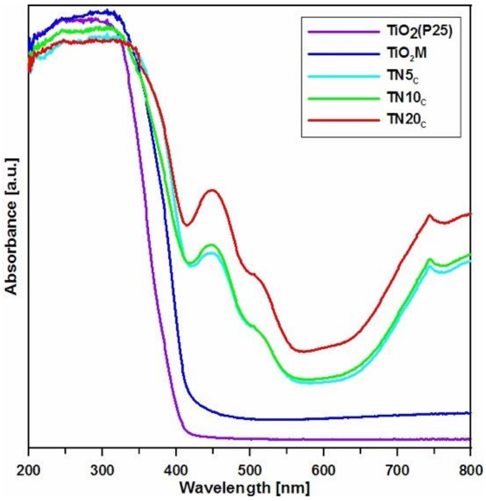

Fig. 10. UV-Vis/DRS spectra of TiO_2 (P25) and obtained samples

Table 6. The band gap energy (E_g) values for TiO_2 (P25) and obtained materials

Sample	Band gap (eV)
TiO_2 (P25)	3.11
TiO_2M	3.05
$TN5_C$	2.94
$TN10_C$	2.97
$TN20_C$	2.98

chemical treatment (TiO_2M, E_g= 3.05 eV) changed the value of the band gap compared to the initial TiO_2 (P25, E_g=3.11 eV). Doping with Ni^{2+} ions changed slightly the band gap values of the materials, however, they showed better photocatalytic properties in the visible light region compared to the initial TiO_2 (P25). Jing et al. (2005) have dopped TiO_2 with Ni^{2+} ions (0-3% wt.). They stated that doping of TiO_2 leads to a constant decrease in the photocatalytic activity. The titanium substitution sites are occupied by Ni^{2+} in the lattice of titania leading to the states of impurity in the energy band gap of the semiconductor (Jing et al., 2005). The dopant not only leads to the response to the visible light in the case of the semiconductor photocatalyst possessing a wide band gap but it acts as a recombination centre resulting in the increased recombination of e^-/h^+ pairs in bulk (Kudo and Sekizawa, 2000). Ni doping is beneficial only in the case the e^-–h^+ pairs recombination on the surface is dominant. When the dopant concentration is high, a charge carrier can be trapped more than once and can be recombined with the next charge carrier. Thus the dopant becomes a center of recombination for the photogenerated e^-/h^+ pairs (Jing et al., 2005). The TiO_2 based materials with nickel ions - 5%, 10% and 15% were obtained by Shaban et al. (2019). According to them the TiO_2 band gap increased with the increasing impurity content. This value was 2.73 eV for pure TiO_2 and 3.16 eV for 15% Ni-doped TiO_2. The doped materials were characterized by smaller photocatalytic activity compared to that of pure TiO_2 (Shaban et al., 2019). Doping of TiO_2 (rutile powder, E_g = 3.03 eV) with nickel ions was also undertaken by Hyun Kim et al., (2006). They prepared a material based on TiO_2 with the addition of Ni (8 wt.%). The material prepared by the mechanochemical alloying and the band gap was E_g = 2.92 eV. This material was characterized by high activity for decomposition of 4-chlorophenol in the aqueous solution at UV and Vis light (Hyun Kim et. al., 2006). Therefore, during the doping of TiO_2, not only the concentration of the dopant but also the method of preparing the photocatalyst play an important role.

4. Conclusions

The structural, thermal and photocatalytic properties of the calcinated materials containing TiO_2 and nickel(II) ions were investigated. The mechanochemical synthesis in the high-energy planetary mill enables simple preparation of photocatalysts without by-products. The data obtained based on the low temperature N_2 adsorption/desorption method indicate that these materials are mesoporous. After calcination of doped materials at 800°C the phase transformation took place. In the composites a small amounts of anatase and dominant amounts of the rutile phase were observed. The obtained materials were characterized by greater photocatalytic activity compared to the initial TiO_2 (P25). The mechanochemical treatment of non-doped titanium dioxide (TiO_2M) increased the efficiency of dye degradation by 10% after 24 hours of irradiation compared to that of initial TiO_2 (P25). The sample with the smallest content of nickel ions $TN5_C$ proved to be the most effective material. After 24 hours in the presence of $TN5_C$ material 68.5% of Safranin T was degraded at visible light. The band gap for this material was E_g = 2.94 eV. In the case of the material with the largest content of Ni^{2+} ions ($TN10_C$, $TN20_C$), the degree of ST was smaller compared to that of the $TN5_C$ material.

References

AJMAL, A., MAJEED, I., MALIK, R. N., IDRISS, H., NADEEM, M. A., 2014. *Principles and mechanisms of photocatalytic dye degradation on TiO_2 based photocatalysts: a comparative overview.* Rsc. Adv. 4(70), 37003-37026.

ALI H., 2010. *Biodegradation of synthetic dyes-a review.* Water, Air, Soil Pollut. 213(1), 251-273.

AMMARI, Y., El ATMANI, K., BAY, L., BAKAS, I., QOURZAL, S., ICHOU, I. A., 2020. *Elimination of a mixture of two dyes by photocatalytic degradation based on TiO_2 P-25 Degussa*. Mater. Today, 22, 126-129.

ANASTAS, P. T., KIRCHHOFF, M. M. 2002. *Origins, current status, and future challenges of green chemistry*. Acc. Chem. Res. 35(9), 686-694.

ANDERSON, C., BARD, A. J., 1995. *An improved photocatalyst of TiO_2/SiO_2 prepared by a sol-gel synthesis*. J. Phys. Chem. 99(24), 9882-9885.

AWUAL, M. R., YAITA, T., MIYAZAKI, Y., MATSUMURA, D., SHIWAKU, H., TAGUCHI, T., 2016. *A reliable hybrid adsorbent for efficient radioactive cesium accumulation from contaminated wastewater*. Sci. Rep. 6(1), 1-10.

BARAKAT, M. A., 2011. *New trends in removing heavy metals from industrial wastewater.* Arab. J. Chem. 4(4), 361-377.

BESSEKHOUAD, Y., ROBERT, D., WEBER, J. V., 2003. *Synthesis of photocatalytic TiO_2 nanoparticles: optimization of the preparation conditions. J.* Photochem. Photobiol. A. 157(1), 47-53.

BHATIA, S.C., 2017. *Pollution control in textile industry*. WPI Publishing, New York.

BURMEISTER, C. F., KWADE, A., 2013. *Process engineering with planetary ball mills.* Chem. Soc. Rev. 42(18), 7660-7667.

CHARMAS, B., SKUBISZEWSKA-ZIĘBA, J., WANIAK-NOWICKA, H., 2017. *Thermal and calorimetric investigations oftitania-silica composites.* Adsorpt. Sci. Technol. 35(7-8), 706-713.

CHAVAN, R. B., 2011. *Environmentally friendly dyes.* Handbook of textile and industrial dyeing, V. 1 in Woodhead Publishing Series in Textiles, *515*-561.

DEAN, J. G., BOSQUI, F. L., LANOUETTE, K. H., 1972. *Removing heavy metals from waste water. Environ.* Sci. Technol. 6(6), 518-522.

DUAN, B., ZHU, Z., SUN, C., ZHOU, J., WALSH, A., 2020. *Preparing copper catalyst by ultrasound-assisted chemical precipitation method.* Ultras. Sonochem. 64, 105013.

DUTTA, K., MUKHOPADHYAY, S., BHATTACHARJEE, S., CHAUDHURI, B., 2001. *Chemical oxidation of methylene blue using a Fenton-like reaction*. J. Hazard. Mater. 84(1), 57-71.

FARGHALI, A. A., ZAKI, A. H., KHEDR, M. H., 2016. *Control of selectivity in heterogeneous photocatalysis by tuning TiO_2 morphology for water treatment applications.* Nanomater. Nanotechnol. 6, 12.

FORGACS, E., CSERHATI, T., OROS, G., 2004. *Removal of synthetic dyes from wastewaters: a review.* Environ. Int. 30(7), 953-971.

GÓRSKA, P., ZALESKA, A., KOWALSKA, E., KLIMCZUK, T., SOBCZAK, J. W., SKWAREK, E., JANUSZ, W., HUPKA, J., 2008. TiO_2 photoactivity in vis and UV light: *The influence of calcination temperature and surface properties.* Appl. Catal. B. Environmental, 84(3-4), 440-447.

GREGG, S. J., SING, K. S. W., 1982. *Adsorption, surface area and porosity.* 2nd ed. Academic Press, London, United Kingdom.

GUN'KO, V.M., 2014. *Composite materials: Textural characteristics*. Appl. Surf. Sci. 307, 444-454.

GUN'KO, V.M., DO, D.D., 2001. *Characterization of pore structure of carbon adsorbents using regularization procedure.* Coll. Surf. A. 19, 71-83.

GUN'KO, V.M., MIKHALOVSKY, S.V., 2004. *Evaluation of slitlike porosity of carbon adsorbents.* Carbon, 42:843-849.

GUTIERREZ, O., PARK, D., SHARMA, K. R., YUAN, Z., 2010. *Iron salts dosage for sulfide control in sewers induces chemical phosphorus removal during wastewater treatment.* Water Res. 44(11), 3467-3475.

HASHIM, K. S., KOT, P., ZUBAIDI, S. L., ALWASH, R., Al KHADDAR, R., SHAW, A., AL-JUMEILY, D., ALJEFERY, M. H., 2020. *Energy efficient electrocoagulation using baffle-plates electrodes for efficient Escherichia Coli removal from wastewater*. J. Water Process. Eng. 33, 101079.

HOLZWARTH, U., GIBSON, N., 2011. *The Scherrer equation versus the'Debye-Scherrer equation*'. Nat. nanotechnol. 6(9), 534-534.

HU, W., LI, L., LI, G., LIU, Y., WITHERS, R. L., 2014. *Atomic-scale control of TiO_6 octahedra through solution chemistry towards giant dielectric response*. Sci. Rep. 4, 6582.

HYUN KIM, D., SUB LEE, K., KIM, Y. S., CHUNG, Y. C., KIM, S. J., 2006. *Photocatalytic Activity of Ni 8 wt%-doped TiO_2 photocatalyst synthesized by mechanical alloying under visible light.* J. Am. Ceram. Soc. 89(2), 515–518.

IQBAL, M. J., ASHIQ, M. N., 2007. *Adsorption of dyes from aqueous solutions on activated charcoal.* J. Hazard. Mater. 139(1), 57-66.

ISMAIL, M., AKHTAR, K., KHAN, M. I., KAMAL, T., KHAN, M. A., M ASIRI, A., JONGCHUL, S., KHAN, S. B., 2019. *Pollution, toxicity and carcinogenicity of organic dyes and their catalytic bio-remediation.* Curr. Pharm. Des. 25(34), 2645-3663.

JING, D., ZHANG, Y., GUO, L., 2005. *Study on the synthesis of Ni doped mesoporous* TiO_2 *and its photocatalytic activity for hydrogen evolution in aqueous methanol solution.* Chemical Physics Letters, 415(1-3), 74-78.

KHAYET, M., 2013. *Treatment of radioactive wastewater solutions by direct contact membrane distillation using surface modified membranes.* Desalination. 321, 60-66.

KOE, W. S., LEE, J. W., CHONG, W. C., PANG, Y. L., SIM, L. C., 2019. *An overview of photocatalytic degradation: photocatalysts, mechanisms, and development of photocatalytic membrane.* Environ. Sci. Pollut. Res. *27*(3), 2522-2565.

KOLEN'KO, Y. V., CHURAGULOV, B. R., KUNST, M., MAZEROLLES, L., COLBEAU-JUSTIN, C., 2004. *Photocatalytic properties of titania powders prepared by hydrothermal method*. Appl. Catal. B. 54(1), 51-58.

KOSOWSKA, B., MOZIA, S., MORAWSKI, A. W., GRZMIL, B., JANUS, M., KAŁUCKI, K., 2005. *The preparation of* TiO_2*–nitrogen doped by calcination of* $TiO_2\cdot xH_2O$ *under ammonia atmosphere for visible light photocatalysis.* Sol. Energy Mater Sol. Cells . 88(3), 269-280.

KUBIAK, A., BIELAN, Z., KUBACKA, M., GABAŁA, E., ZGOŁA-GRZEŚKOWIAK, A., JANCZAREK, M., ZALAS, M., ZIELIŃSKA-JUREK, A., SIWIŃSKA-CIESIELCZYK, K. JESIONOWSKI, T., 2020. *Microwave-assisted synthesis of a* TiO_2*-CuO heterojunction with enhanced photocatalytic activity against tetracycline.* Appl. Surf. Sci. 520, 146344.

KUCIO, K., CHARMAS, B., PASIECZNA-PATKOWSKA, S., 2019. *Structural, thermal and photocatalytic properties of composite materials* $SiO_2/TiO_2/C$. Adsorption. 25(3), 501-511.

KUCIO, K., CHARMAS, B., PASIECZNA-PATKOWSKA, S., ZIĘZIO, M., 2020. *Mechanochemical synthesis of nanophotocatalysts* $SiO_2/TiO_2/Fe_2O_3$*: their structural, thermal and photocatalytic properties.* Appl. Nanosci. 10, 4733-4746.

KUDO, A., SEKIZAWA, M., 2000. *Photocatalytic* H_2 *evolution under visible light irradiation on Ni-doped ZnS photocatalyst.* Chem. Commun. 15, 1371-1372.

LONG, Q., ZHANG, Z., Qi, G., WANG, Z., CHEN, Y., LIU, Z. Q., 2020. *Fabrication of chitosan nanofiltration membranes by the film casting strategy for effective removal of dyes/salts in textile wastewater.* ACS Sustain. Chem. Eng. 8(6), 2512-2522.

LOPEZ, R., GÓMEZ, R., 2012. *Band-gap energy estimation from diffuse reflectance measurements on sol–gel and commercial* TiO_2*: a comparative study*. J. Sol-Gel Sci. Technol. 61(1), 1-7.

MAHAPATRA, N.N., 2016. *Woodhead Publishing India in Textiles. Textile Dyes.* CRC Press, New Delhi.

MOLCHANOV, V.V., BUYANOV, R.A., 2001. *Scientific grounds for the application of mechanochemistry to catalyst preparation*. Kinet. Catal. 42(3), 366–374.

NEGISHI, N., TAKEUCHI, K., 1999. *Structural changes of transparent* TiO_2 *thin films with heat treatment.* Mater. Lett. 38(2), 150-153.

NICHIO, N. N., CASELLA, M. L., PONZI E. N., FERRETTI, A. O. A., 2003. *Study of the decomposition of supported nickel acetylacetonate by thermal techniques.* Thermochim. Acta, 400(1-2), 101-107.

PANDIT, A. B., KUMAR, J. K., 2019. *Drinking water treatment for developing countries: physical, chemical and biological pollutants.* R. Soc. Chem., Croydon, United Kingdom.

QDAIS, H. A., MOUSSA, H., 2004. *Removal of heavy metals from wastewater by membrane processes: a comparative study.* Desalination, 164(2), 105-110.

RAUF, M. A., ASHRAF, S. S., 2009. *Fundamental principles and application of heterogeneous photocatalytic degradation of dyes in solution.* Chem. Eng. J. 151(1-3), 10-18.

ROUQUEROL, J., BARON, G., DENOYEL, R., GIESCHE, H., GROEN, J., KLOBES, P., LEVITZ, P., NEIMARK, A.V., RIGBY, S., SKUDAS, R., SING, K., THOMMES, M., UNGER, K., 1994. *Recommendations for the characterization of porous solids.* Pure. Appl. Chem. 66, 1739-1758.

SAINI, R. D., 2017. *Textile organic dyes: polluting effects and elimination methods from textile waste water.* Int. J. Chem. Eng. Res. 9(1), 121-136.

SANCHEZ-MARTINEZ, A., CEBALLOS-SANCHEZ, O., KOOP-SANTA, C., LÓPEZ-MENA, E. R., OROZCO-GUAREÑO, E., GARCÍA-GUADERRAMA, M., 2018. *N-doped* TiO_2 *nanoparticles obtained by a facile coprecipitation method at low temperature*. Ceram. 44(5), 5273-5283.

SHABAN, M., AHMED, A. M., SHEHATA, N., BETIHA, M. A., RABIE, A. M., 2019. *Ni-doped and Ni/Cr co-doped* TiO_2 *nanotubes for enhancement of photocatalytic degradation of methylene blue. J.* Colloid Interface Sci. 555, 31-41.

SOCRATES, G., 2001. *Infrared and Raman characteristic group frequencies. Tables and charts.* John Wiley&Sons, Ltd., Chichester, England.

SYDORCHUK, V., KHALAMEIDA, S., SKWAREK, E., BIEDRZYCKA, A., *2022. Some applications of barium titanate prepared by different methods*. Physicochem. Probl. Miner. Process., 58(2), 147192.

TAN, B. H., TENG, T. T., OMAR, A. M., 2000. *Removal of dyes and industrial dye wastes by magnesium chloride.* Water res. 34(2), 597-601.

TAN, K. B., VAKILI, M., HORRI, B. A., POH, P. E., ABDULLAH, A. Z., SALAMATINIA, B., 2015. *Adsorption of dyes by nanomaterials: recent developments and adsorption mechanisms.* Sep. Purif. Technol. 150, 229-242.

TÜRGAY, O., ERSÖZ, G., ATALAY, S., FORSS, J., WELANDER, U., 2011. *The treatment of azo dyes found in textile industry wastewater by anaerobic biological method and chemical oxidation.* Sep. Purif. Technol. 79(1), 26-33.

VISWANATHAN, B., 2018. *Photocatalytic degradation of dyes: an overview.* Current Catalysis, 7(2), 99-121.

ZALESKA, A., 2008. *Doped-*TiO_2*: A Review.* Recent Pat. Eng. 2(3), 157-164.

ZHOU, C. S., WU, J. W., DONG, L. L., LIU, B. F., XING, D. F., YANG, S. S., WU, X. K., WANG, Q., FAN, J. N., FENG, L. P., CAO, G. L., 2020. *Removal of antibiotic resistant bacteria and antibiotic resistance genes in wastewater effluent by UV-activated persulfate.* J. Hazard. Mater. 388, 122070.